Upper Bound Solution for the Stability of Surcharged Soil Slope Using Nonlinear Failure Criterion

Aminpour, M.M.[1] and Maleki, M.[2]*

[1] Ph.D., Civil Engineering Department, Bu-Ali Sina University, Hamedan, Iran.
[2] Associate Professor, Civil Engineering Department, Bu-Ali Sina University, Hamedan, Iran.

ABSTRACT: In this paper using the upper bound limit analysis method, the stability of soil slope, uniformly surcharged at the crest is investigated. According to the soil behavior at the failure state, a continuous failure criterion nonlinear function of confining stress, and soil initial density is considered. The stress field along the slip surface is entered into the limit analysis formulation according to the Airy stress function. The ultimate uniformly distributed load is obtained by optimizing the virtual work equation. The effects of different parameters such as slope angle, soil unit weight, and initial density are investigated. Considering the nonlinear effects of confining stresses leads to a reduction in the ultimate load. This reduction is more obvious in slopes with lower angles. According to the proposed formulation, with increasing soil density, the ultimate load of the slope stability is increased. The results for different slope angles are compared with those obtained from the limit equilibrium-based methods. The ultimate loads of the proposed method are in some cases lower and in some cases more than the results of different methods based on limit equilibrium.

Keywords: Airy Stress Function, Nonlinear Failure Criterion, Slope Stability, Upper Bound Limit Analysis Method.

1. Introduction

The construction of footing on the crest of a slope has a significant effect on its stability. In the technical literature, there are many studies dedicated to loading on the slopes, slope stability, and bearing capacity of footing near the slope. In general, the analytical approaches to this problem can be divided into three categories of limit equilibrium (Vo and Russell, 2017; Shukla and Jakka, 2018; Hajiazizi et al., 2018; Mirzazadeh and Hajiazizi, 2020; Hu et al., 2022; Tozato et al., 2022), method of characteristics and limit analysis (Mofidi et al., 2014; Tang et al., 2015; Qin and Chain, 2018; Zhou et al., 2018; Froutan Kalourazi et al., 2019, Guanhua, 2023; Zhou and Qin, 2023). In addition, several experimental studies (e.g. Hajiazizi and Nasiri, 2019; Razali et al., 2023; Thomas et al., 2023) have been performed in this field.

The stability of surcharged slopes using the limit analysis technique was studied by several researchers (e.g. Mofidi Rouchi, 2014; Tang et al., 2015; Haghbin and

---

* Corresponding author E-mail: maleki@basu.ac.ir

Ghazavi, 2016; Vo and Russell, 2017; Qin and Chin, 2017, 2018; Aminpour et al., 2017, 2018; Aminpour and Maleki, 2022). Tang et al. (2015) presented some practical charts for assessing the slope stability in different loading conditions taking into account the effect of pore water pressure. Vo and Russell (2017) studied the slope stability of nonhomogeneous unsaturated slopes subjected to uniform loading using the limit equilibrium technique. Qin and Chain (2017, 2018) discretized the log-spiral failure wedge into vertical slices and calculated the ultimate load applied to the slope.

Using the limit analysis technique, Aminpour et al. (2017, 2018) investigated the effect of surcharge on the behavior of soil slopes under various seismic conditions and soil reinforcement. Aminpour and Maleki (2022) estimated the bearing capacity of strip footing on the slope by using finite element limit analysis technique considering nonlinear continuous failure criterion with a non-associated flow rule. Tran et al. (2019) investigated the stability of the slope with the foundation during rainfall using a finite difference program. Komasi and Beiranvand (2022) investigated the stability analysis of earth dam under drawdown conditions. In this study, the finite element method was used to study the seepage from the body of the earth dam.

The majority of the above-mentioned studies are based on Mohr-Coulomb (MC) failure criterion. In the limit analysis technique, upon using the MC criterion, the stress fields do not affect the rate of dissipated energy. In this case, the rate of internal work will only depend on cohesion and will be obtained by multiplying cohesion by the tangential component of the velocity vector (Chen, 1975).

A considerable number of studies show that almost all geomaterials obey nonlinear failure criteria. On this basis, different non-linear failure surfaces have been proposed and applied for stability analysis in geotechnical problems (e.g. Maleki et al., 2000; Liu and Carter, 2003; Baker, 2004;

Sun and Song, 2016; Wu et al., 2017).

In the present research, using the upper bound limit analysis, the ultimate uniformly distributed load adjacent to a slope is investigated. Instead of the non-continuous MC criterion, the continuous criterion of CJS (Maleki et al., 2000) is used. In this criterion, the failure state is a nonlinear function of confining pressure and material density. The stress components along the slip surface are determined based on chosen Airy function. To find the critical condition, the virtual work is subjected to unconstrained nonlinear optimization in the MATLAB program. Finally, the results are compared with those of the slices methods.

2. The Log-Spiral Rotational Failure Mechanism

The slope undergoes a shear failure with a rotational log-spiral failure mechanism due to building loading (Figure 1). In this study, for simplicity and by ignoring the stiffness of the building, the load of the building is replaced by an infinite uniformly distributed load. The soil wedge will fail around point O with an angular velocity of $\dot{\Omega}$. The equation of log-spiral failure surface can be written as Eq. (1), in which, $R(\theta)$: is the radius of an arbitrary angle θ and $u(\theta)$: is the velocity that depends on $R(\theta)$ and can be obtained from Eq. (2).

$$R(\Theta) = R_0 \exp(\Theta - \Theta_0) \qquad (1)$$
$$u(\Theta) = R\dot{\Omega} = R_0\, exp(\Theta - \Theta_0)\dot{\Omega} \qquad (2)$$

3. Stress Field in the Soil Mass in Polar Coordinates

In the upper bond solution, the plastic deformation rate is related to the stress components through the flow rule ($\dot{\varepsilon}_{ij}^{p} = \lambda\, \partial f / \partial \sigma_{ij}$). Therefore, the stress components in the slip log spiral bond of the failure mechanism must be known as a function of coordinate variables. By considering perfectly plastic behavior for material, stress components in the plastic state remain constant. The stress

components in this state can be considered as components obtained at the beginning of yielding. At this point, kinematic and equilibrium equations accompanied by isotropic linear elasticity constitutive equations, lead to a solution for determining the stress components.

In the theory of elasticity, the stresses applied to the soil mass can be expressed by Eq. (3) using the Airy stress function. In this equation, $\varphi(r,\theta)$ is the Airy stress function in polar coordinates. It is assumed that the body force is derivable from a scalar potential $\hat{V}$. In the polar coordinates, $\hat{V}$ can be expressed by Eq. (4).

$$\begin{cases} \sigma_{rr} = \sigma_{rr}(r,\theta) = \dfrac{1}{r}\dfrac{\partial\varphi}{\partial r} + \dfrac{1}{r^2}\dfrac{\partial^2\varphi}{\partial\theta^2} + V \\[2mm] \sigma_{\theta\theta} = \sigma_{\theta\theta}(r,\theta) = \dfrac{\partial^2\varphi}{\partial r^2} + V \\[2mm] \sigma_{r\theta} = \tau_{r\theta} = \tau_{r\theta}(r,\theta) = -\dfrac{\partial}{\partial r}\left(\dfrac{1}{r}\dfrac{\partial\varphi}{\partial\theta}\right) \end{cases}$$

(3)

$$\hat{V} = \gamma\, r\sin\theta$$

(4)

The Airy stress function is written in polar coordinated (Sadd, 2009) as follows.

$$\varphi(r,\theta) = r^2(c_1 + c_2\theta + c_3\,sin2\theta + c_4\,cos2\theta)$$

(5)

Substituting Eq. (5) into Eq. (3), the stress components in polar coordinates can be obtained as following expressions.

$$\begin{aligned} \sigma_{rr} &= 2c_1 + 2c_2\theta + 2c_3\sin2\theta \\ &\quad + 2c_4\cos2\theta \\ &\quad -4c_3\sin2\theta - 4c_4\cos2\theta + \gamma\, r\sin\theta \\ \sigma_{\theta\theta} &= 2c_1 + 2c_2\theta + 2c_3\sin2\theta \\ &\quad + 2c_4\cos2\theta + \gamma\, r\sin\theta \\ \sigma_{r\theta} &= -c_2 - 2c_3\cos2\theta + 2c_4\sin2\theta \end{aligned}$$

(6)

Initially, the center of polar coordinates is considered at the edge of the slope. The geometry of the problem in polar coordinate, center of rotation, and slip surface are shown in Figure 2.

Boundary conditions on the ground surface and along the slope are expressed in Eq. (7) where L: is the length of failure wedge on the ground surface.
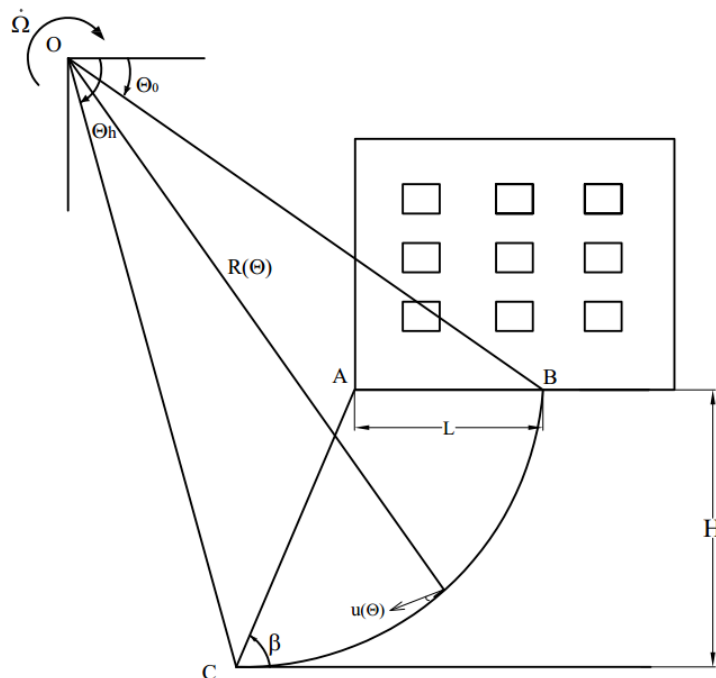
Fig. 1. The rotational failure mechanism with a surcharge due to uniform loading adjacent to the slope
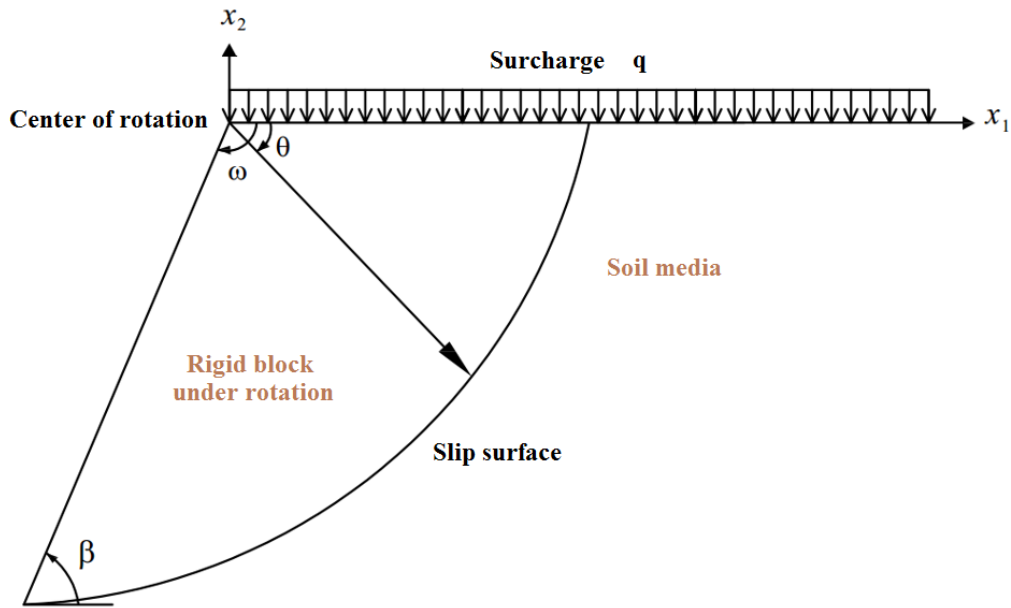
Fig. 2. Cartesian and polar coordinates considered in the present research

$$\theta = 0, \quad \begin{array}{ll} \sigma_{r\theta} = 0 & \Rightarrow \quad -c_2 - 2c_3 = 0 \\ \sigma_{\theta\theta} = q & \Rightarrow \quad 2c_1 + 2c_4 = q \end{array}$$

$$\theta = \omega, \quad \begin{array}{l} \sigma_{r\theta} = 0 \Rightarrow -c_2 - 2c_3\cos2\omega \\ \quad +2c_4\sin2\omega = 0 \\ \sigma_{\theta\theta} = 0 \Rightarrow 2c_1 + 2c_2\omega + \\ 2c_3\sin2\omega + 2c_4\cos2\omega + \gamma\,r\sin\omega \\ \quad = 0 \end{array}$$

$$\omega = \pi - \beta, \quad r = r_0\exp(\theta - \theta_0) = L\exp(\theta) \tag{7}$$

Finally, solving the above equations, the constants of the Airy stress function are obtained as follows.

$$c_1 = \frac{q}{2} - c_4, \qquad c_2 = -2c_3$$

$$c_3 = -\frac{q + \gamma\,r\sin\omega}{2(1 + \cos2\omega) - \dfrac{2\sin2\omega}{1 - \cos2\omega}(2\omega - \sin2\omega)}$$
$$\times \frac{\sin2\omega}{1 - \cos2\omega}$$

$$c_4 = \frac{q + \gamma\,r\sin\omega}{2(1 + \cos2\omega) - \dfrac{2\sin2\omega}{1 - \cos2\omega}(2\omega - \sin2\omega)} \tag{8}$$

4. Nonlinear Failure Criteria

The Mohr-Coulomb failure criterion has

been widely used in upper-bound solutions of geotechnical problems. Mohr-Coulomb criterion, for a given internal friction angle, considers a linear relationship between shear strength and normal stress. Besides, the effect of density has not been automatically provided so that, for a given problem, the internal friction angle must be identified based on medium density. However, based on experimental observation, the failure state in soils is a nonlinear function of confining pressure as well as soil density. Besides, lack of intermediate principal stress in Mohr-Coulomb led to discontinuity of the failure surface relative to the stress components.

In the present study, the failure surface equation of the CJS elastoplastic constitutive model is used as the failure criterion for identifying upper bond solution. This model has been originally proposed for predicting the stress-strain behavior of granular soils (Cambou et al., 1989). The failure surface of the CJS model was then extended based on experimental observations in order to improve its prediction (Maleki et al., 2000). The general form of CJS failure surface for granular materials is given by:

$$f(\sigma) = s_{II}h(\theta) - R_m I_1 = 0 \tag{9}$$

in which, $s_{II} = \sqrt{s_{ij} s_{ij}}$: represents the second invariant of the deviatoric stress tensor of s_{ij} with $s_{ij} = \sigma_{ij} - \frac{\sigma_{kk}}{3} \delta_{ij}$, $I_1 = \sigma_{kk}$: is the first invariant of the stress tensor, R_m: illustrates the mean radius of the failure surface and the function $h(\theta)$: controls the geometrical form of failure surface about hydrostatic axis in stresses space with the following expression.

$$h(\theta) = (1 - \gamma \cos 3\theta)^{1/6}$$
$$= \left[1 - \sqrt{54}\gamma \frac{det(s_{ij})}{s_{II}^3} \right]^{1/6} \quad (10)$$

where θ: is Lode's angle and γ: is a constant parameter of the model. The choice of γ depends on material behavior at the failure state.

As seen from Figure 3a, for $\gamma = 0$ a circular form of failure surface is achieved in the deviatoric stresses plane, however, choosing a value greater than zero for γ leads to an asymmetric form of failure surface about the hydrostatic axis. In the present study, by considering $\gamma = 0$, a simplified form of the failure surface of the CJS model with the following expression was used.

$$f(\sigma) = s_{II} - R_m I_1 = 0 \quad (11)$$

Based on the experimental observations, the shear strength of the granular soils at the peak state depends on the confining stress and soil density. In the CJS failure surface, these issues have been well described in the framework of critical state soil mechanics. The mean radius of the failure surface R_m in Eq. (11), is a function of stress level and soil density and varies between a maximum initial value (R_{mi}) corresponding to peak resistance to a minimum value ($R_{critical}$) related to the critical state resistance.

$$R_m = R_{critical} + (R_{mi} - R_{critical})(1 - \frac{I_1}{3p_c})^\alpha \quad (12)$$

The critical state pressure p_c depends on the soil density through an exponential relationship (Maleki et al., 2000). According to the experimental observations concerning the stress-strain behavior of granular soils at peak and post-peak states α has been fixed equal to 1.5 (Bathayian and maleki, 2018). A typical soil stress-strain curve is shown in Figure 3b. The maximum and critical state mean radii (R_{mi} and $R_{critical}$) of the failure surface, are related to point A (peak state) and point B (critical state) respectively. The manner of determination of CJS criterion parameters has been given in Maleki et al. (2000). Intersecting CJS and Mohr-Coulomb criteria in axisymmetric triaxial conditions results in the direct relationships for R_{mi} and $R_{critical}$ in terms of internal friction angle at peak and critical states, respectively, which are presented in Appendix A.2 (Eqs. (A2-1 and A2-2)).
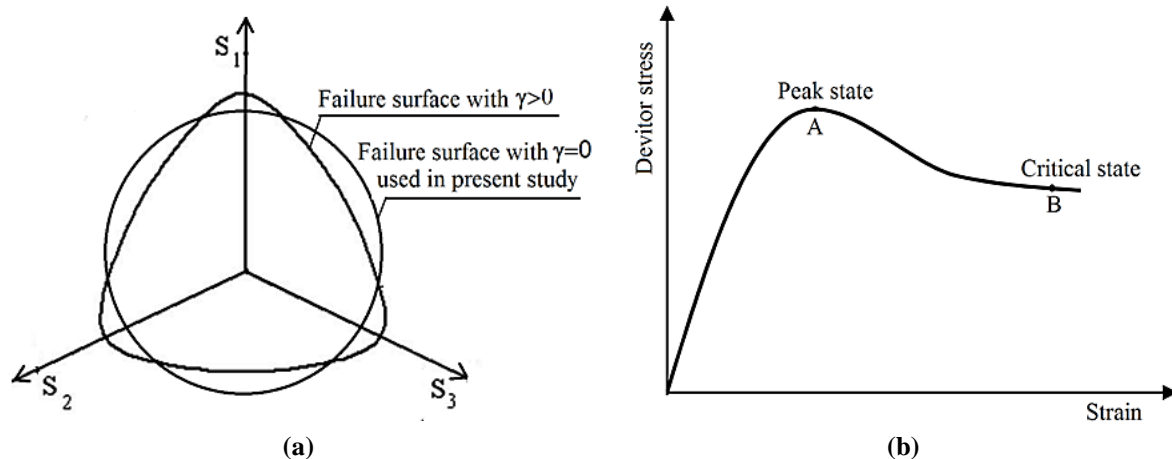

| (a) | (b) |

Fig. 3. a) CJS failure surface in deviatoric stress space; and b) Schematic deviator stress-strain behavior of soil

5. Internal Power Dissipation

Based on the upper bound limit analysis theorem and virtual work equation, by setting the rate of external work equal to the rate of internal Power dissipation, obtained loads in this field will not be smaller than the actual failure loads. The mathematical form of the virtual work equation can be written as follows.

$$\iint_{\bar{V}} \sigma_{ij}\,\dot{\varepsilon}_{ij}dV = \iint_V b_i\,u_i dV + \iint_{S_t} T_i\,u_i dS_t \tag{13}$$

where σ_{ij}: is the state of stress and $\dot{\varepsilon}_{ij}$: is the rate of plastic strain. The internal power dissipation is equal to the product of the stress tensor and plastic strain rate. T_i: is the unknown distributed load on the boundaries S_t and b_i: is the body force on the volume V and u_i: is the incipient velocity in the selected mechanism. The stress components are identified depending on the failure mechanism geometry and considered Airy function. The second invariant of the deviatoric stress tensor of the CJS failure criterion in plane strain conditions are defined as follows.

$$\begin{aligned} s_{II} &= \sqrt{s_{ij}s_{ij}} \\ &= \sqrt{s_{11}^2 + s_{22}^2 + s_{33}^2 + 2s_{12}^2} \\ &= \sqrt{s_{rr}^2 + s_{\theta\theta}^2 + s_{33}^2 + 2s_{r\theta}^2}\,\sigma_3 \\ &= v(\sigma_{rr} + \sigma_{\theta\theta})I_1 = \sigma_{rr} + \sigma_{\theta\theta} + \sigma_3 \end{aligned} \tag{14}$$

The CJS failure surface in S_{II}-I_1 coordinates has a nonlinear form as illustrated in Figure 4. In this figure, the shear strain rate, $\dot{e}_{II}$, versus volumetric strain rate, $\dot{\varepsilon}_V$, is also shown. Based on the normality rule, the dilation angle of ξ can be expressed in terms of stress state by differentiation of failure surface as follows.

$$\begin{aligned} \frac{ds_{II}}{dI_1} = \tan\xi = (R_{mi} \\ - R_{critical})\Big(1 \\ - \frac{I_1}{3p_c}\Big)^\alpha \Big(\frac{\alpha}{3p_c}\Big(1 \\ - \frac{I_1}{3p_c}\Big)^{\alpha-2}(I_1) - 1\Big) \\ + R_{critical} \end{aligned} \tag{15}$$

According to Figure 5, if t: is the thickness of the region including discontinuity of velocity, the shear strain can be obtained by dividing the tangential velocity by this thickness. Therefore, the increment of dissipated internal energy in the unit area of discontinuous surfaces is defined as Eq. (16).

$$d\dot{D} = (s_{II}\dot{e}_{II} - I_1\dot{\varepsilon}_v)(t \times 1 \times 1) \tag{16}$$

Based on Figure 4 and the expression of the dilation angle, the increment of dissipated internal energy is defined as follows.

$$\begin{aligned} \dot{\varepsilon}_v &= \tan\xi\,\dot{e}_{II} \\ d\dot{D} &= (s_{II} - I_1\tan\xi)\dot{e}_{II}\ (t \times 1 \times 1) \\ &= (s_{II} - I_1\tan\xi)\,(\delta u) \end{aligned} \tag{17}$$

The dissipated internal energy is adopted based on a center coordinate at the edge of the slope (local coordinates). In order to establish the virtual work equation, the dissipated energy has to be defined based on the center of the global coordinates at the rotational log-spiral outside of the slope. The local coordinates (x_1, x_2, r, θ), as well as the global coordinates (X_1, X_2, R, Θ) are shown in Figure 6. The transformation matrix is expressed as the following form.

$$\begin{pmatrix} \cos(R,r) & \cos(R,\theta) \\ \cos(\theta,r) & \cos(\Theta,\theta) \end{pmatrix} = \begin{pmatrix} \cos\eta & \sin\eta \\ \sin\eta & -\cos\eta \end{pmatrix} \tag{18}$$

As shown in Figure 6, the angle η: is defined as $\theta - \Theta$ by extending the radius, r. According to this figure, the relationship

between the polar angles of two coordinate systems can be obtained as shown in Eqs. (19) and (20), respectively. The r_0 is equal to the length of failed soil mass on the ground, L.

$$R\sin\Theta = R_0\sin\Theta_0 + r\sin\theta$$
$$\rightarrow \exp(\Theta - \Theta_0)\sin\Theta =$$
$$\sin\Theta_0 + \frac{r_0}{R_0}\exp(\theta)\sin\theta$$
$$R_0\cos\Theta_0 - R\cos\Theta + r\cos\theta = L \quad (19)$$
$$\rightarrow \exp(\Theta - \Theta_0)\cos\Theta =$$
$$\cos\Theta_0 + \frac{r_0}{R_0}\exp(\theta)\cos\theta - \frac{L}{R_0}$$

$$\Theta = $$
$$\tan^{-1}\left(\frac{\sin\Theta_0 + \frac{r_0}{R_0}exp(\theta)\sin\theta}{\cos\Theta_0 + \frac{r_0}{R_0}exp(\theta)\cos\theta - \frac{L}{R_0}}\right)\eta$$
$$= \theta - \Theta \quad (20)$$

By transforming the local coordinates to the global coordinates, the limit stresses in global coordinates are identified for establishing the virtual work equation.

$$\begin{pmatrix} \sigma_{RR} & \sigma_{R\Theta} \\ \sigma_{R\Theta} & \sigma_{\Theta\Theta} \end{pmatrix} =$$
$$\begin{pmatrix} \cos\eta & \sin\eta \\ \sin\eta & -\cos\eta \end{pmatrix} \times \begin{pmatrix} \sigma_{rr} & \sigma_{r\theta} \\ \sigma_{r\theta} & \sigma_{\theta\theta} \end{pmatrix} \times \quad (21)$$
$$\begin{pmatrix} \cos\eta & \sin\eta \\ \sin\eta & -\cos\eta \end{pmatrix}^T$$

or,

$$\sigma_{RR} = \sigma_{rr}\cos^2\eta + \sigma_{\theta\theta}\sin^2\eta$$
$$+\sigma_{r\theta}\sin2\eta$$
$$\sigma_{\Theta\Theta} = \sigma_{rr}\sin^2\eta + \sigma_{\theta\theta}\cos^2\eta$$
$$-\sigma_{r\theta}\sin2\eta \quad (22)$$

$$\sigma_{R\Theta} = 0.5\sigma_{rr}\sin2\eta - 0.5\sigma_{\theta\theta}\sin2\eta$$
$$+\sigma_{r\theta}(\sin^2\eta - \cos^2\eta)$$

The stress invariants are also expressed as follows.

$$s_{II} = \sqrt{s_{RR}^2 + s_{\Theta\Theta}^2 + s_{33}^2 + 2s_{R\Theta}^2}$$
$$I_1 = \sigma_{RR} + \sigma_{\Theta\Theta} + \sigma_{33}$$
$$\sigma_{33} = \upsilon\ (\sigma_{RR} + \sigma_{\Theta\Theta})$$
$$s_{RR} = \frac{2\sigma_{RR} - \sigma_{\Theta\Theta} - \sigma_{33}}{3}$$
$$s_{\Theta\Theta} = \frac{2\sigma_{\Theta\Theta} - \sigma_{RR} - \sigma_{33}}{3} \quad (23)$$
$$s_{33} = \frac{2\sigma_{33} - \sigma_{RR} - \sigma_{\Theta\Theta}}{3}$$
$$s_{R\Theta} = \sigma_{R\Theta} - \frac{\sigma_{RR} + \sigma_{\Theta\Theta} + \sigma_{33}}{3}$$

The rate of total dissipated energy is obtained by integrating the increments of dissipated energy along the log-spiral slip surface.

$$\dot{D} = \int_{\Theta_0}^{\Theta_h}(s_{II} - I_1\tan\xi)(\delta u)\,Rd\Theta$$
$$= \int_{\Theta_0}^{\Theta_h}R_0^2(s_{II} - I_1\tan\xi)$$
$$\times exp[2(\Theta - \Theta_0)]\,\dot{\Omega}d\Theta \quad (24)$$
$$= \int_{\Theta_0}^{\Theta_h}R_0^2(s_{II} - I_1\tan\xi)$$
$$\times exp[2(\Theta - \Theta_0)]\,\dot{\Omega}\frac{d\Theta}{d\theta}\,d\theta$$

where the shear velocity is based on the global coordinates. The stresses are also transformed from the local coordinates to the global coordinates.
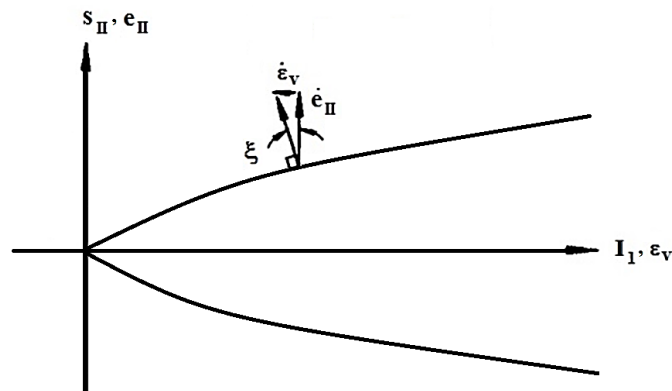

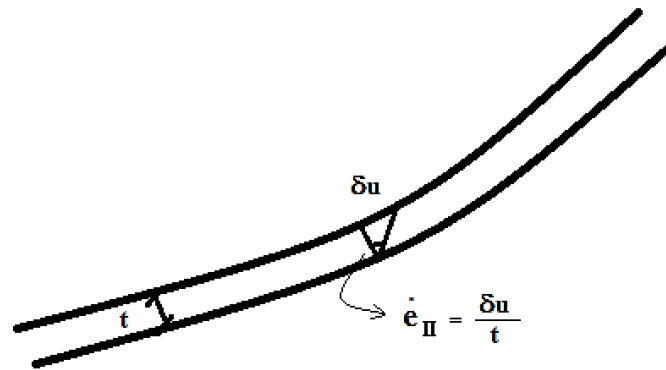**Fig. 4.** CJS failure line in S_{II}-I_1 coordinates

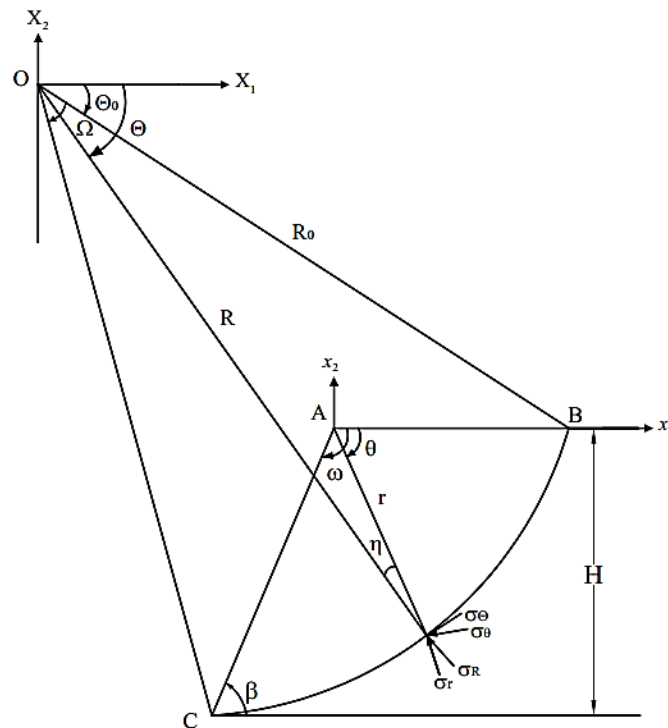**Fig. 5.** Differential discontinuity in the slip surface

Fig. 6. Coordinate transformation and polar stress components applied at the failure state

6. The Ultimate Load

The rate of external work due to the weight of the failure wedge can be obtained from Eq. (25). In this equation, the functions f_1, f_2, and f_3 are defined in Appendix A.1 (Eqs. (A1-1 and A1-2)) (Chen, 1975). The rate of work done by the uniform surcharge adjacent to the slope is obtained from Eq. (26) by multiplying the moment of surcharge by the rotational velocity.

$$\dot{W} = \gamma R_0^3 \dot{\Omega}(f_1 - f_2 - f_3) \qquad (25)$$

$$\dot{Q} = qL \left(R_0 \cos \Theta_0 - \frac{L}{2} \right) \dot{\Omega} \qquad (26)$$

At the onset of failure, the dissipated internal energy is equal to the rate of external work. By minimizing the virtual work equation, the ultimate uniform load, q, is obtained. It has to be noted that the rate of external work done by surcharge and dissipated energy is obtained based on the unknown, q.

$$min \;\; \dot{D} - \dot{W} - \dot{Q} \;\; on(\Theta_0, \Theta_h, q) \qquad (27)$$

The virtual work equation is subjected to unconstrained nonlinear optimization. For this purpose, numerical methods such as fminsearch or fminunc optimization in the MATLAB program or repetitive loops on the Θ_0, Θ_h angle, and surcharge can be used. Therefore, by writing codes in MATLAB

programming language, the minimum ultimate uniform load can be obtained.

7. Results of the Proposed Formulation

In order to analyze the formulation and extract the uniform load, a 4 m slope with geotechnical properties listed in Table 1 was assumed. The values of R_{mi} and $R_{critical}$ were identified regarding internal friction angles at peak and critical states based on the relationships presented in the Appendix. It should be noted that, for simplicity in the optimization process, p_c was fixed as a constant parameter of p_{c0}.

In the presented formulation, an infinite uniform surcharge was considered. So, the length of the failure surface on the ground was not predefined. This length can be deduced as one result of optimization of Eq. (27). Table 2 shows different values of the length of failure surface, start and end angles around the center of rotation, and ultimate load on different slopes for nonlinear CJS method and variable R_m.

The nonlinear dependence of the failure state of soils on confining pressure has been well introduced in the formulation of the CJS failure criterion, so increasing confining pressure leads to a decrease in the rate of shear strength augmentation. Figure 7 shows the variations of the ultimate load in terms of slope angle for different maximum surface failure radii. In this analysis, the nonlinear CJS method has been used and, with the constant parameters in Table 1, the maximum failure radius has been changed. As can be observed in this figure, as the failure surface radius is increased, the ultimate load is also increased for all values of slope angles. Besides, for a given failure surface radius, while the slope angle is increased, the ultimate load is augmented. The rate of decrease in the ultimate load due to an increase in slope angle augments with an increase in the failure surface radius.

In order to study the effect of confining pressure on ultimate load, a constant mean radius of the failure surface equal to its

maximum value, R_{mi}, was assumed and the results were compared with the case in which the radius is variable. As can be observed in Figure 8, for the fixed radius, the ultimate load is always greater than when the variable radius is used. For the slope angle equal to 30 degrees, a smaller difference in results is observed. The analysis with constant R_m is related to the upper bond solution in which shear strength varies as a linear function of stress level. It should be noted that the majority of existing works concerning the upper bond solution of slope stability have used Mohr-Coulomb or Drocker-Prager criteria. The results of the analysis with constant R_m presented in Figure 8 are similar to the upper bond solution of surcharged slopes stability based on the Drocker-Prager criterion because parameter γ in the CJS criterion is assumed to be zero.

Figure 9 shows variations of the ultimate load versus the initial critical state stress for different slope angles. This parameter is related to the initial density of granular soil. The large values of initial critical state pressure correspond to the high values of relative density. By increasing the initial critical state stress, p_{c0}, the ultimate load has been increased. According to Figure 9, the maximum difference between the ultimate loads for the initial critical stresses of 200 and 2000 kPa is about 160 kPa on a slope of 30 degrees.

Variations of the ultimate load versus soil unit weight for different slope angles are shown in Figure 10. By increasing the soil unit weight, the ultimate load is increased. The rate of decrease in the ultimate load by increasing slope angle is maximum in the unit weight, $\gamma = 20$ kN/m^3 compared to other conditions. By increasing the unit weight, the stresses and the effect of confining stress have increased.

In the following, the results of the proposed method are compared with the equilibrium method of GeoSlope software (2007). The GeoSlope software is a subset of the GeoStudio software and the slope stability analysis in this program is

performed by studying the equilibrium of the vertical slices of the soil mass. In this regard, various methods of slices including the Ordinary method of the slice, Bishop's method, Janbu's generalized method, and Morgenstern-Price method are used.

The factor of safety of a slope is defined as the ratio of the available shear strength of the soil to the minimum shear strength required to maintain stability. In the GeoSlope software, the shear strength of soils for effective stress analysis is governed by the Coulomb failure criterion. The proposed formulation is in the limit state and in this case, the factor of safety is equal to one.

In Figure 11, the performed model in the GeoSlope software is shown. The slope has, a height of 4 m and an angle of 30°. Besides, a specific weight of 18 kN/m^3, internal friction angle of 37°, and zero cohesion was considered. The intensity of the surcharge in this figure is equivalent to the ultimate load extracted from the proposed formulation in Table 2. In this figure, the critical failure wedge and the center of its rotation are shown for the Morgenstern-

Price method. The factor of safety in the Morgenstern-Price method is 0.946.

Figure 12 shows the comparison between the factors of safety in various methods. The values obtained from the proposed method with the CJS failure criterion are among the values obtained from the various methods of slices based on the Mohr-Coulomb failure criterion. The results of different slices methods at a 30° slope are always less than the ultimate load value of the proposed method. However, with the decrease of the slope, the amount of ultimate load resulting from the different methods of slices has increased. At 20° slope angle, the results of the Ordinary method and Janbu's generalized method are lower than the proposed method and the results of Bishop's method and Morgenstern-Price method are more than the proposed method. At 10° slope angle, the results of slices methods are always more than the proposed method. The factor of safety at 10° slope angle in the Ordinary method is 1.005 which is very close to the results obtained from the proposed method.
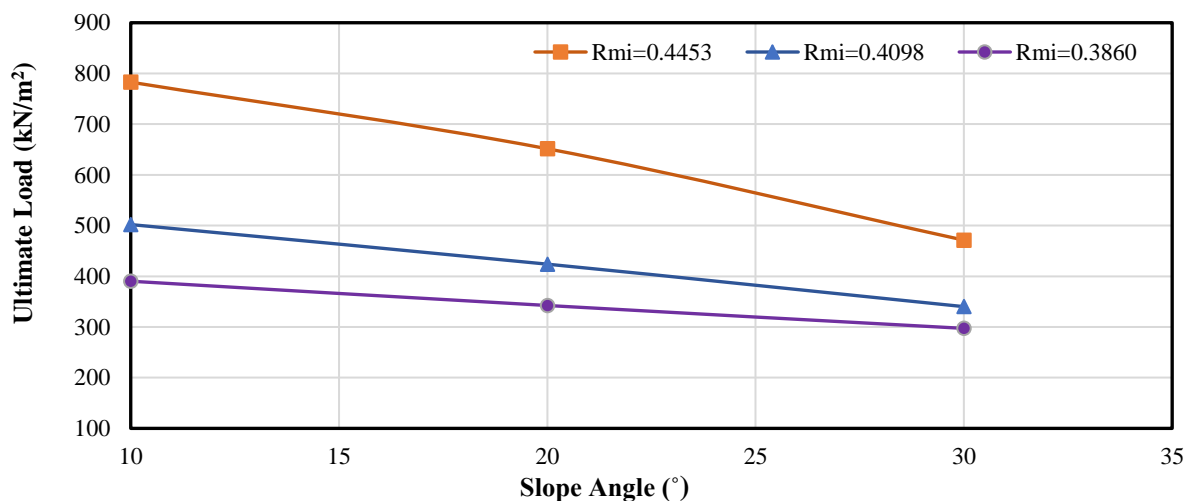

Fig. 7. Variations of the ultimate load versus angle of slope in different failure surface radii

Table 1. Geotechnical properties of slope material

P_{c0} (kPa)	$R_{critical}$	R_{mi}	$\phi_{critical}$ (°)	ϕ_{peak} (°)	υ	γ (kN/m^3)
1000	0.3503	0.4098	32	37	0.35	18

Table 2. Optimization results obtained from the suggested method

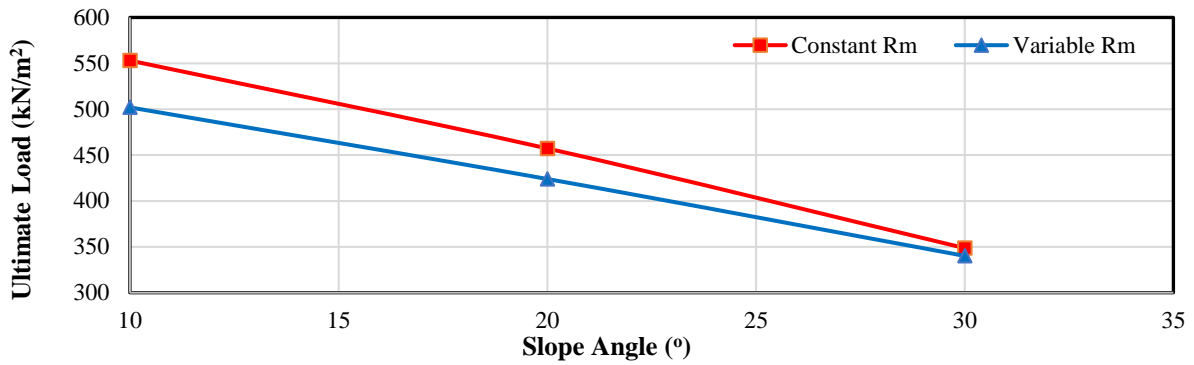| q_u (kPa)	L (m)	L/H	Θ_h (°)	Θ_0 (°)	H (m)	β (°)
501.93	1.05	0.262	155.6	77.6	4	10
423.88	1.51	0.433	145.5	74.3	4	20
340.08	2.43	0.607	138.8	71.9	4	30

Fig. 8. Comparison between the ultimate load in fixed and variable failure surface radius
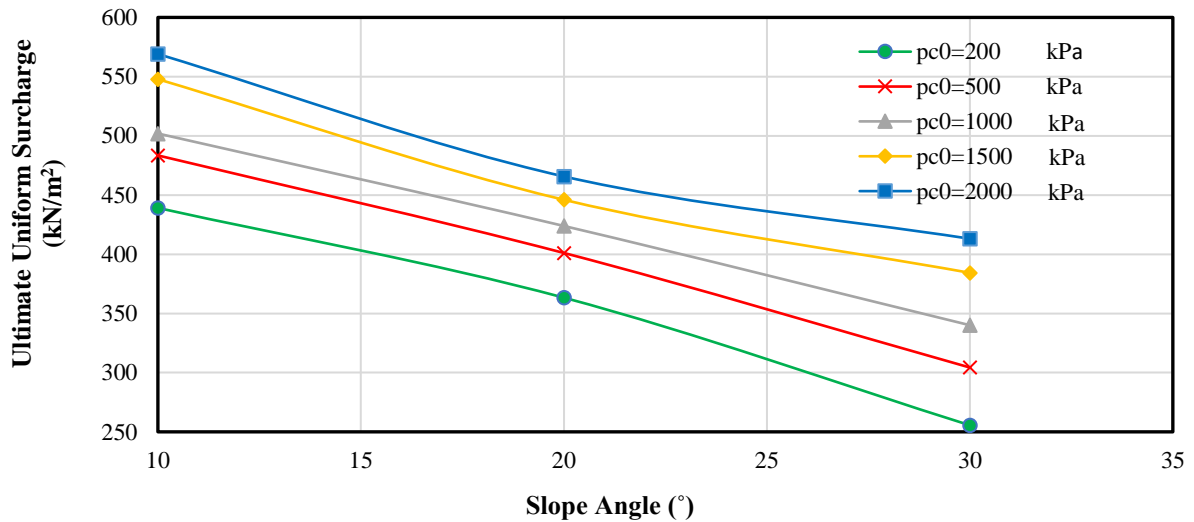

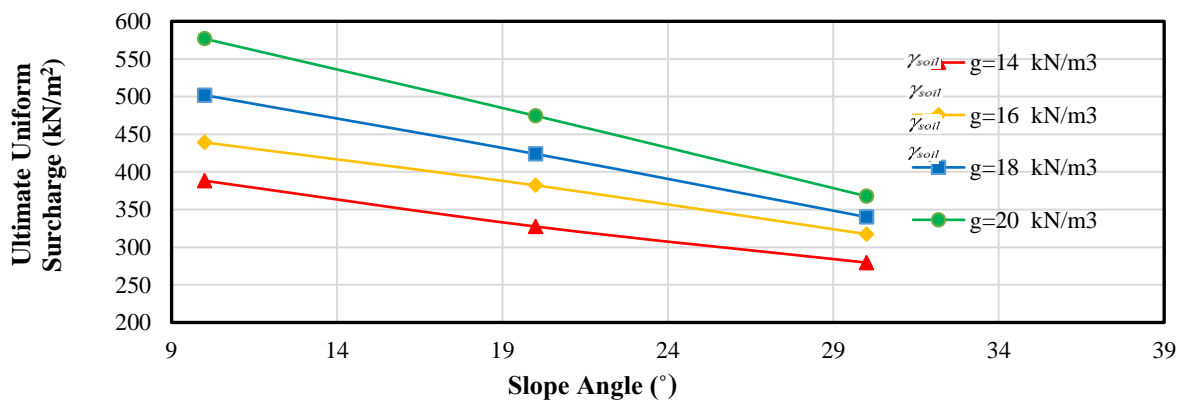**Fig. 9.** Effect of initial critical state stress on the ultimate load in terms of slope angle

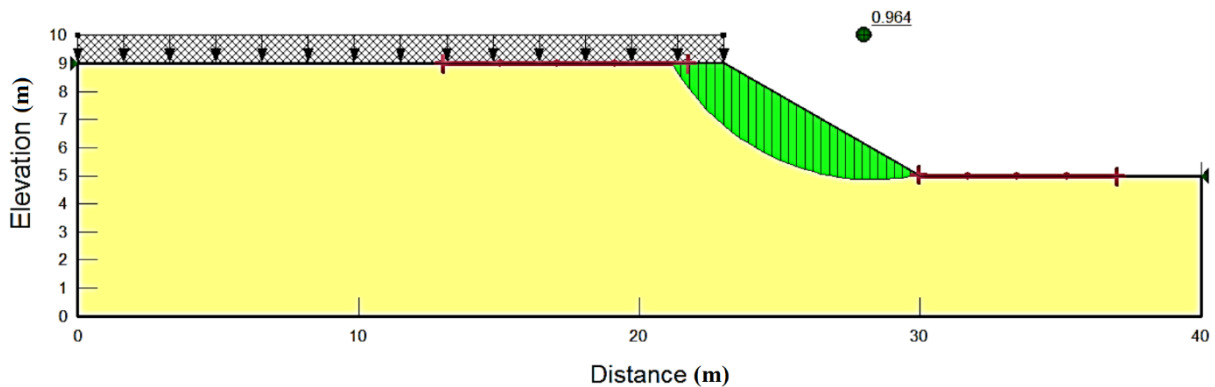**Fig. 10.** Variations of the ultimate load versus angle of slope in different unit weights

Fig. 11. Critical failure wedge and factor of safety in the GeoSlope software
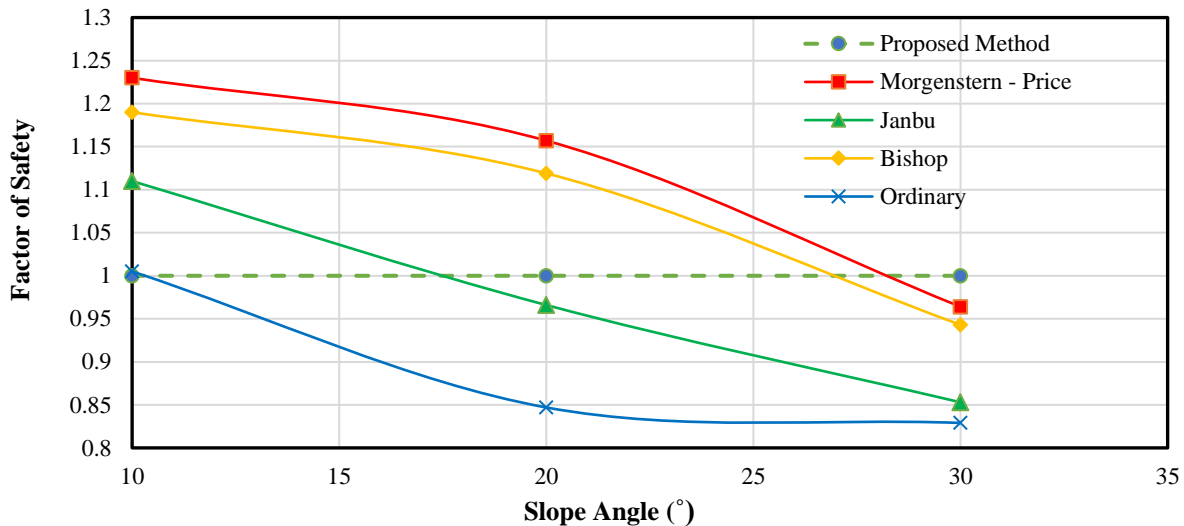
Fig. 12. Comparison between the results of the present study with those of the slices methods

8. Conclusions

In this paper using a continuous failure criterion as a nonlinear function of confining stress and soil density, formulation of the upper bound limit analysis method for estimating the ultimate uniform load adjacent to a slope was presented. In order to estimate the rate of dissipated internal energy, the stress field along the slip surface was determined in polar coordinates based on the Airy stress function.

Taking into account the nonlinear effect of confining pressure in the analyses, led to a decrease in the ultimate load. This reduction was more obvious in slopes with smaller angles. An increase in the radius of the soil failure criterion caused an increase in the ultimate load. This increase was more significant in slopes with lower angles.

With a set of failure state parameters, the ultimate load was affected by the change in soil initial density, so the increase of initial density led to a rise in the ultimate load. Using the presented failure criterion resulted in a more accurate estimation of the soil behavior.

The results of the proposed method were compared with different slices methods based on the Mohr-Coulomb failure criterion. The suggested limit analysis technique results in greater values for ultimate load at a 30° slope angle and

smaller values at a 10° slope angle compared to different methods of slices.

The analysis with a constant mean radius of the failure surface is related to the upper bond solution in which shear strength varies as a linear function of stress levels such as Mohr-Coulomb and Drocker-Prager criteria. A considerable difference was observed between the results of analyses with constant and variable mean radii of the failure surface.

9. References

Aminpour, M.M., Maleki, M. and Ghanbari, A. (2017). "Investigation of the effect of surcharge on behavior of soil slopes", *Geomechanics and Engineering*, 13(4), 653-669, https://doi.org/10.12989/gae.2017.13.4.653.

Aminpour, M.M., Maleki, M. and Ghanbari, A. (2018), "Predicting seismic permanent displacement of soil walls under surcharge based on limit analysis approach", *Earthquake Engineering and Engineering Vibration*, 17(4), 747-759, https://doi.org/10.1007/s11803-018-0473-6.

Aminpour, M.M. and Maleki, M. (2022). "Finite Element limit analysis using nonlinear continuous failure criterion and non-associated flow rule and its application to estimating bearing capacity of strip footing on slope", *Geotechnical and Geological Engineering,* 40, 723-734.

Baker, R. (2004). "Nonlinear Mohr envelopes based on triaxial data", *Journal Geotechnial and Geoenvironmental Engineering*, 130(5), 498-506, https://doi.org/10.1061/(ASCE)1090-0241(2004)130:5(498).

Bathayian, M.H. and Maleki, M. (2018). "Adaptation of an existing constitutive model for describing mechanical behaviour of cemented granular soils", *Geomechanics and Geoengineering an International Journal*, 13(3), 184-197, https://doi.org/10.1080/17486025.2018.143424 3.

Cambou, B., Jafari, K. and Elamrani, K. (1989). "An elastoplastic model for granular material using three yielding mechanisms", Numerical Models in Geomechanics, NUMOG III, Proceedings of the 3rd International Symposium, Niagara Falls, Canada, (pp. 149-167).

Chen, W.F. (1975). *Limit analysis and soil plasticity*, Elsevier Science, Amsterdam, Netherlands.

Froutan Kalourazi, A., Izadi, A. and Jamshidi Chenari, R. (2019). "Seismic bearing capacity of shallow strip foundations in the vicinity of slopes using the lower bound finite element method", *Soils and Foundations*, 59(6), 1891-1905, https://doi.org/10.1016/j.sandf.2019.08.014.

Guanhua, Q. (2023). "Stability analysis of nonhomogeneous and anisotropic stepped slopes under the influence of earthquakes", *Heliyon,* 9(4), e15057, https://doi.org/10.1016/j.heliyon.2023.e15057.

Haghbin, M. and Ghazavi M. (2016). "Seismic bearing capacity of strip footings on pile-stabilized slopes", Civil *Engineering Infrastructure Journal*, 49(1), 111-126, https://doi.org/10.1061/(ASCE)GM.1943-5622.0002530.

Hajiazizi, M., Kilanehei, P. and Kilanehei, F. (2018). "A new method for three-dimensional stability analysis of earth slopes", *Scientia Iranica*, 25(1), 129-139, https://doi.org/10.24200/sci.2017.4173.

Hajiazizi, M., Mazaheri, A.R. and Orense, R.P. (2018). "An analytical approach to evaluate stability of pile-stabilized slope", *Scientia Iranica*, 25(5), 2525-2536, https://doi.org/10.24200/sci.2017.4218.

Hajiazizi, M. and Nasiri, M. (2019). "Experimental and numerical investigation of reinforced sand slope using geogird encased stone column", *Civil Engineering Infrastructures Journal*, 52(1), 85-100, https://doi.org/10.22059/ceij.2019.253069.1468.

Hu, L., Takahashi, A. and Kasama, K. (2022). "Effect of spatial variability on stability and failure mechanisms of 3D slope using random limit equilibrium method", *Soils and Foundations*, 62(6), 101225, https://doi.org/10.1016/j.sandf.2022.101225.

Komasi, M. and Beiranvand, B. (2021). "Seepage and stability analysis of the Eyvashan Earth Dam under drawdown conditions", *Civil Engineering Infrastructures Journal,* 54(2), 205-223, https://doi.org/10.22059/ceij.2020.293429.1634.

Liu, M.D. and Carter, J.P. (2003). "General strength criterion for geomaterials", *International Journal of Geomechanics*, 3(2), 253-259, https://doi.org/10.1061/(ASCE)1532-3641(2003)3:2(253).

Maleki, M., Dubujet, Ph. and Cambou, B. (2000). "Modélisation Hierarchisée du comportement des sols", *Revue Francais de Genie Civil*, 4(7-8), 895-928, https://doi.org/10.1080/12795119.2000.969270 2.

Mirzazadeh, Z. and Hajiazizi, M. (2020). "Determination of creep-induced displacement of soil slopes based on LEM", *Civil Engineering Infrastructures Journal*, 53(2), 341-358, https://doi.org/10.22059/ceij.2020.285244.1598.

Mofidi Rochi, J., Farzaneh, O. and Askari, F. (2014). "Bearing capacity of strip footings near slopes using lower bound limit analysis", *Civil Engineering Infrastructures Journal*, 47(1), 89-109, https://doi.org/10.7508/CEIJ.2014.01.007.

Qin, C. and Chian, S.C. (2017). "Kinematic stability of a two-stage slope in layered soils", *International Journal of Geomechanics*, 17(9), https://doi.org/10.1061/(ASCE)GM.1943-5622.0000928.

Qin, C. and Chian, S.C. (2018). "Bearing capacity analysis of a saturated non-uniform soil slope with discretization-based kinematic analysis", *Computers and Geotechnics*, 96, 246-257, https://doi.org/10.1016/j.compgeo.2017.11.003.

Razali, I.H., Taib, A.M., Rahman, N.A., Abang Hasbollah, D.Z., Mohd Firdaus Md Dan, M.F., Ramli, A.B. and Ibrahim, A. (2023). "Slope stability analysis of riverbank in Malaysia with the effects of vegetation", *Physics and Chemistry of the Earth*, Parts A/B/C, 129, 103334, https://doi.org/10.1016/j.pce.2022.103334.

Sadd, M.H. (2009). *Easticity: Theory, applications and numerics*, 2nd Edition, Elsevier, Academic Press, Burlington, MA, USA, Oxford, UK.

Shukla, R.P. and Jakka R.S. (2018). "Critical setback distance for a footing resting on slopes under seismic loading", *Geomechanics and Engineering*, 15(6), 1193-1205, https://doi.org/10.12989/gae.2018.15.6.1193.

Sun, Y. and Song, E. (2016). "Active earth pressure analysis based on normal stress distribution function along failure surface in soil obeying nonlinear failure criterion", *Acta Geotechnica*, 11(2), 255-268, https://doi.org/10.1007/s11440-015-0390-z.

Tang, G., Zhao, L., Li, L. and Yang, F. (2015). "Stability charts of slopes under typical conditions developed by upper bound limit analysis", *Computers and Geotechnics*, 65, 233-240, https://doi.org/10.1016/j.compgeo.2014.12.008.

Thomas, J., Gupta, M. and Prusty, G. (2023). "Assessing global parameters of slope stability

model using Earth data observations for forecasting rainfall, Induced shallow landslides", *Journal of Applied Geophysics*, 212, 104994, https://doi.org/10.1016/j.jappgeo.2023.104994.

Tozato, K.J., Dolojan, N.L., Touge, Y., Kure, S., Moriguchi, S., Kawagoe, S., Kazama, S. and Terada, K. (2022). "Limit equilibrium method-based 3D slope stability analysis for wide area considering influence of rainfall", *Engineering Geology*, 308, 106808, https://doi.org/10.1016/j.enggeo.2022.10680 8.

Tran, A.T.P., Kim, A.R. and Cho, G.C. (2019). "Numerical modeling on the stability of slope with foundation during rainfall", *Geomechanics and Engineering*, 17(1), 109-118, https://doi.org/10.12989/gae.2019.17.1.109.

Vo, T. and Russell, A.R. (2017). "Stability charts for curvilinear slopes in unsaturated soils", *Soils and Foundations*, 57(4), 543-556, https://doi.org/10.1016/j.sandf.2017.06.005.

Wu, S., Zhang, S., Guo, C. and Xiong, L. (2017). "A generalized nonlinear failure criterion for frictional materials", *Acta Geotechnica*, 12(6), 1353-1371, https://doi.org/10.1007/s11440-017-0532-6.

Zhou, H., Zheng, G., Yin, X., Jia, R. and Yang, X. (2018). "The bearing capacity and failure mechanism of a vertically loaded strip footing placed on the top of slopes", *Computers and Geotechnics*, 94, 12-21, https://doi.org/10.1016/j.compgeo.2017.08.009.

Zhou, J. and Qin, C. (2023). "Influence of soft band on seismic slope stability by finite-element limit-analysis modelling", *Computers and Geotechnics,* 158, 105396.

A. Appendix

A.1. Determination of Coefficients *f1, f2* and *f3*

The coefficients f_1, f_2, and f_3 are the rate of external work done in log spiral OBC and two OAB and OAC triangles in Figure 6, respectively (Chen, 1975). These coefficients can be written as the following equations. Also, according to the geometry shown in Figure 6, the parameters L and R_0 can be expressed based on Θ_h and Θ_o (Chen, 1975).

$$f_1(\Theta_0, \Theta_h) = \frac{1}{30}((3\cos\Theta_h + \sin\Theta_h)$$
$$\times \exp[3(\Theta_h - \Theta_0)] - 3\cos\Theta_0 - \sin\Theta_0)$$
$$f_2(\Theta_0, \Theta_h) = \frac{1}{6}\frac{L}{R_0}\left(2\cos\Theta_0 - \frac{L}{R_0}\right)\sin\Theta_0$$

$$f_3 = \frac{1}{6}\exp(\Theta_h - \Theta_0) \quad \text{(A1-1)}$$
$$\times (\sin(\Theta_h - \Theta_0) - \frac{L}{R_0}\sin\Theta_h)$$
$$\times (\cos\Theta_0 - \frac{L}{R_0} + \cos\Theta_h \exp(\Theta_h - \Theta_0))$$

$$\frac{L}{R_0}$$
$$= \frac{1}{\sin\Theta_h}\left[\sin(\Theta_h - \Theta_0) \right.$$
$$\left. - \frac{H}{R_0}\frac{\sin(\beta + \Theta_h)}{\sin\beta}\right] \quad \text{(A1-2)}$$
$$\frac{H}{R_0} = \sin\Theta_h \exp(\Theta_h - \Theta_0)$$
$$- \sin\Theta_0$$

A.2. Relation between Failure Surface Radius and Soil Internal Friction Angle

By intersecting the two MC and CJS failure criteria, the following relationships exist between the maximum and critical state failure surfaces radii and the internal friction angle of the soil at peak and critical states (Maleki et al., 2000).

$$R_{mi} = 2\sqrt{\frac{2}{3}\frac{\sin\varphi_{peak}}{3 - \sin\varphi_{peak}}} \quad \text{(A2-1)}$$

$$R_{critical} = 2\sqrt{\frac{2}{3}\frac{\sin\varphi_{critical}}{3 - \sin\varphi_{critical}}} \quad \text{(A2-2)}$$